Crystal Orientation and Grain Size: Do They Determine Optoelectronic Properties of $MAPbI_3$ Perovskite?

Loreta A. Muscarella[1], Eline M. Hutter[1], Sandy Sanchez[2], Christian D. Dieleman[1], Tom J. Savenije[3], Anders Hagfeldt[2], Michael Saliba[4,5], Bruno Ehrler[1,*]

[1] Center for Nanophotonics, AMOLF, Science Park 104, 1098 XG Amsterdam, The Netherlands

[2] Laboratory of Photomolecular Science (LSPM) École Polytechnique Fédérale de Lausanne (EPFL), Station 6, 1015 Lausanne, Switzerland

[3] Department of Chemical Engineering, Delft University of Technology, Van der Maasweg 9, 2629 HZ Delft, The Netherland

[4] Institute of Materials Science Technical University of Darmstadt Alarich-Weiss-Strasse 2, D-64287 Darmstadt, Germany

[5] IEK-5 Photovoltaik, Forschungszentrum Jülich GmbH, 52425 Jülich, Germany

Corresponding Author*

b.ehrler@amolf.nl

Supplementary Figures

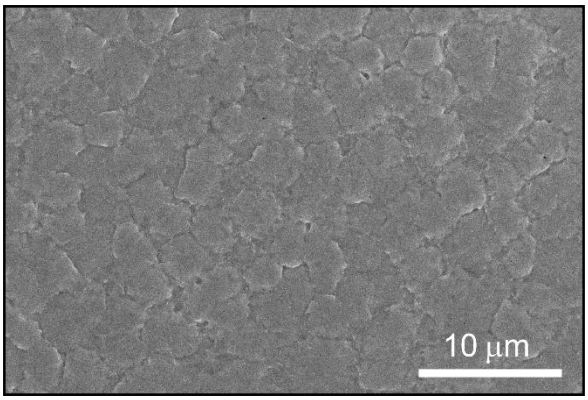

Figure S1. SEM images of $MAPbI_3$ fabricated via antisolvent dripping at lower magnification. SEM shows perovskite domains of micron size.

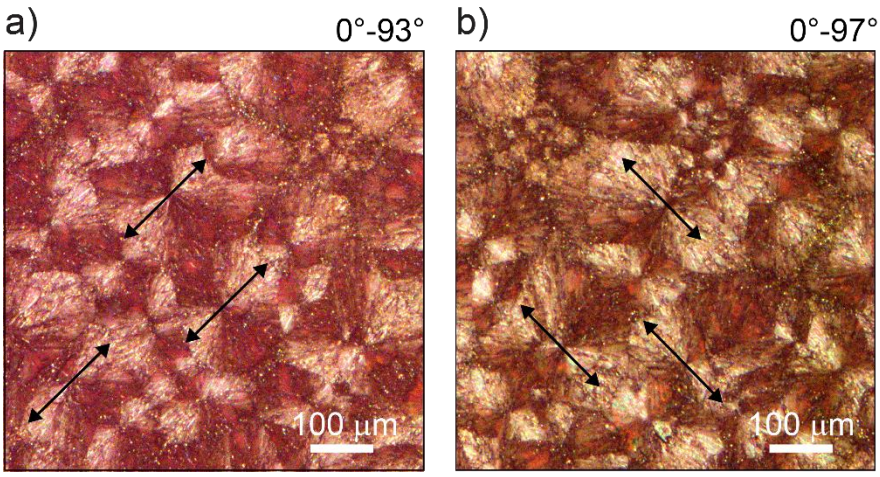

Figure S2. Polarized light microscopy of the same area of FIRA sample deposited on quartz. Analyser and polarizer are set at **a)** 0° and 93° and **b)** 0° and 97° degree, respectively. The perovskite shows a birefringent behaviour typical of spherulitic crystals.

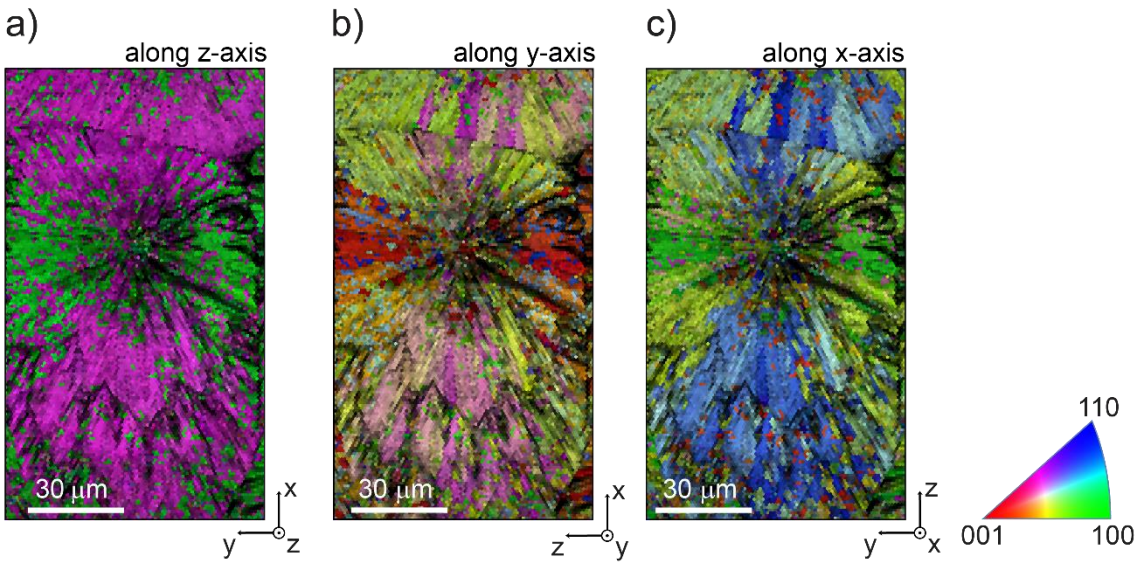

Figure S3. Image Quality (IQ) overlay with Inverse Pole Figure (IPF) map of the FIRA sample showing crystallographic orientation along **a)** z-direction, **b)** y-direction and **c)** x-direction. The perovskite domains that show homogeneous orientation along all three directions correspond to a crystallographic grain.

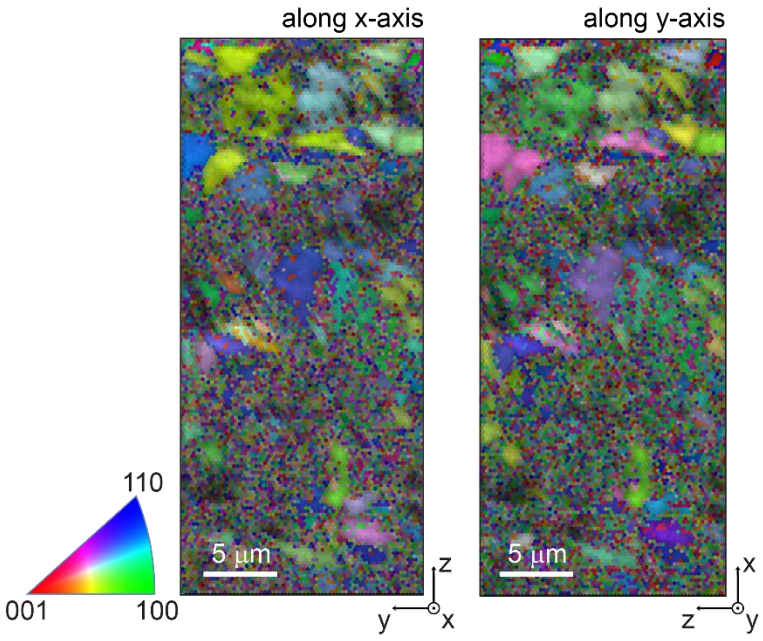

Figure S4. Image Quality (IQ, brightness) overlay with Inverse Pole Figure (IPF) map of AS sample showing crystallographic orientation along x-direction and y-direction. The perovskite domains that show homogeneous orientation along x-, y-, and z-direction correspond to a crystallographic grain.

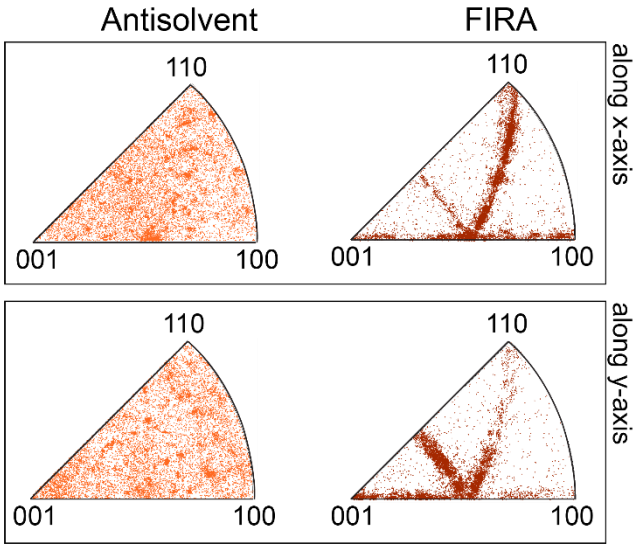

Figure S5. Crystal orientation distribution along x-, y- and z-axis for AS and FIRA system. The AS system shows almost random orientation along the three directions while the FIRA system shows preferential orientation.

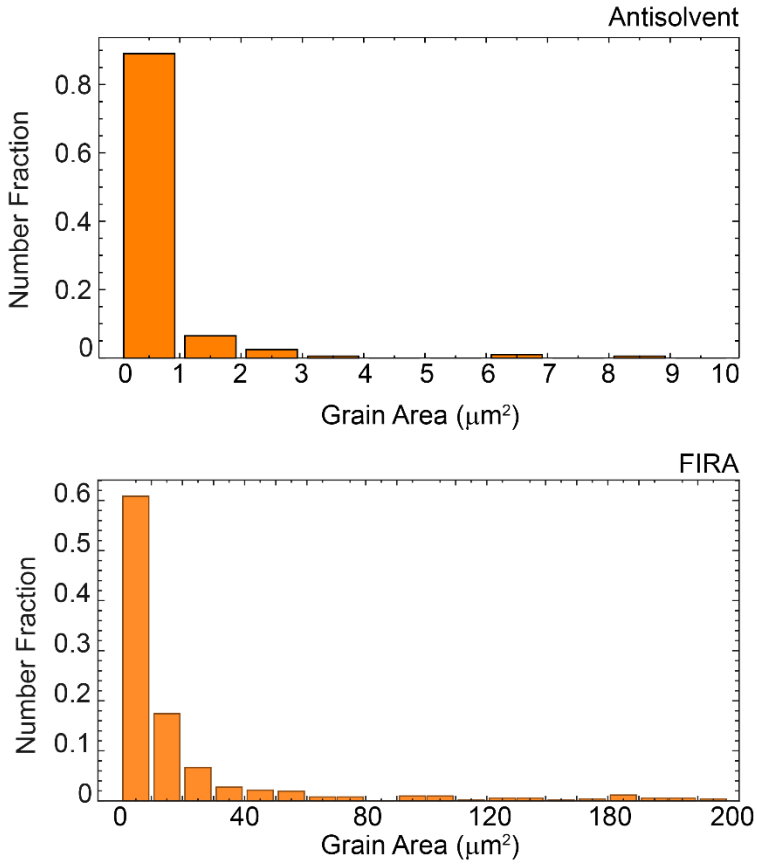

Figure S6. Grain area obtained from EBSD measurements in the AS and FIRA system. For the AS sample the binning in the histogram is 1 μm^2 and for the FIRA sample is 10 μm^2.

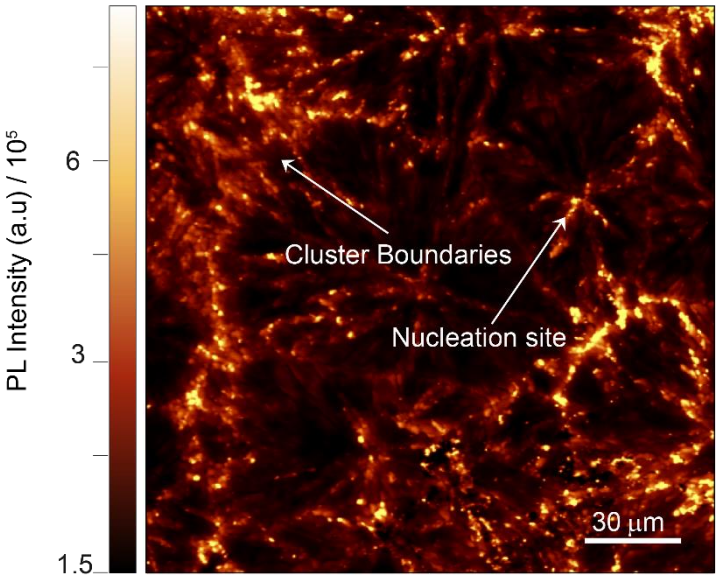

Figure S7. Spatially resolved PL of a bigger region of the FIRA sample including several clusters with a resolution of 0.33µm per pixel. This map shows the enhancement in PL at the CBs and nucleation site for all the clusters. The enhancement varies from 4 to 6 times.

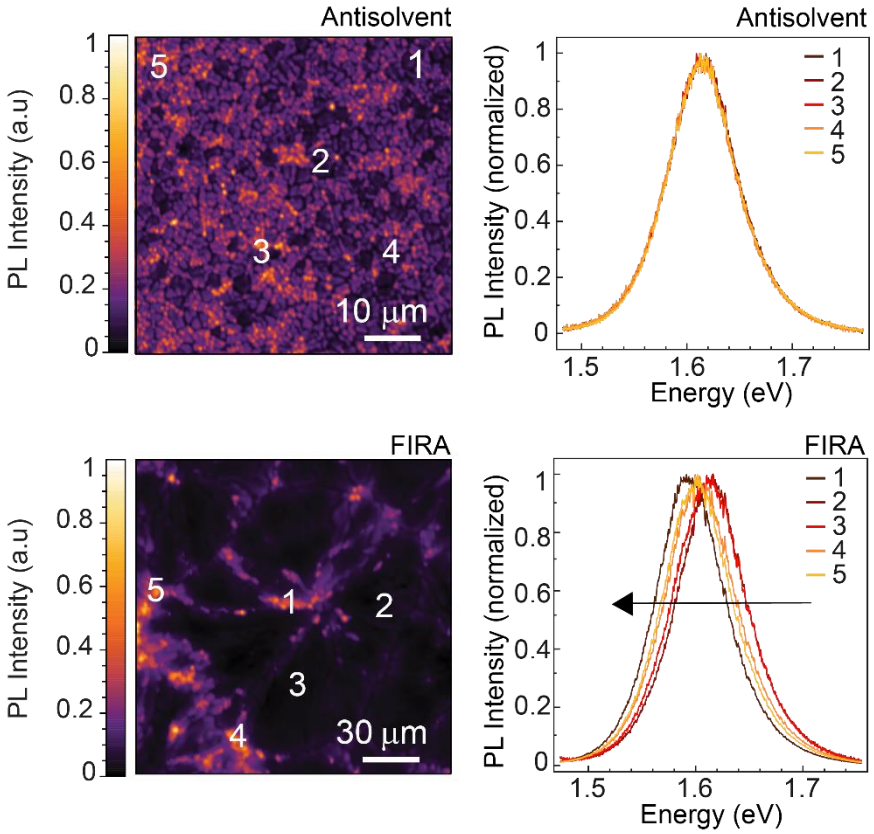

Figure S8. Normalized PL of the five regions highlighted in the main text for the AS and FIRA sample. The peak position in the AS sample remains constant in different regions showing no asymmetry in the emission peak, whereas in the FIRA sample the PL peak is red-shifted and more asymmetric moving from the interior region of the cluster (**Point 2&3**), to the CBs (**Point 4&5**) to the nucleation site (**Point 1**).

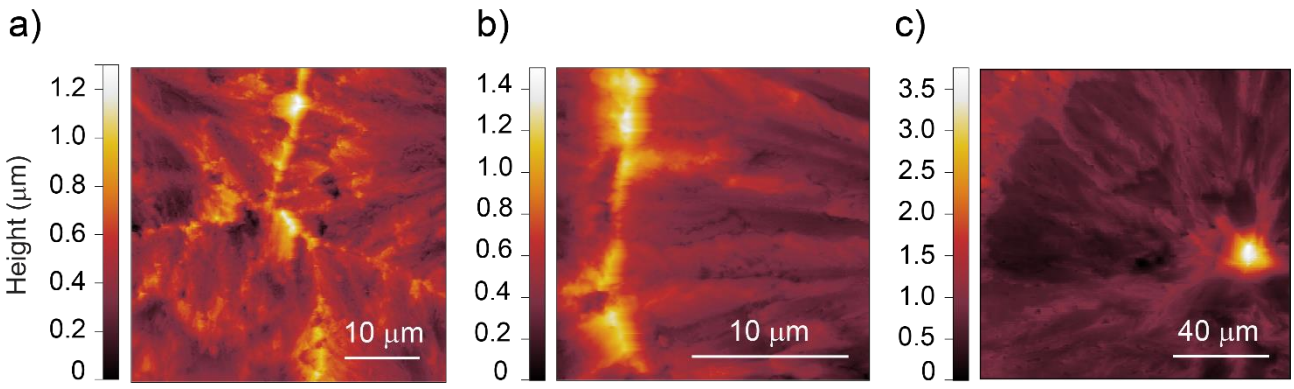

Figure S9. AFM images of FIRA sample at two different regions at the CBs **(a,b)** and at the nucleation site **(c)**.

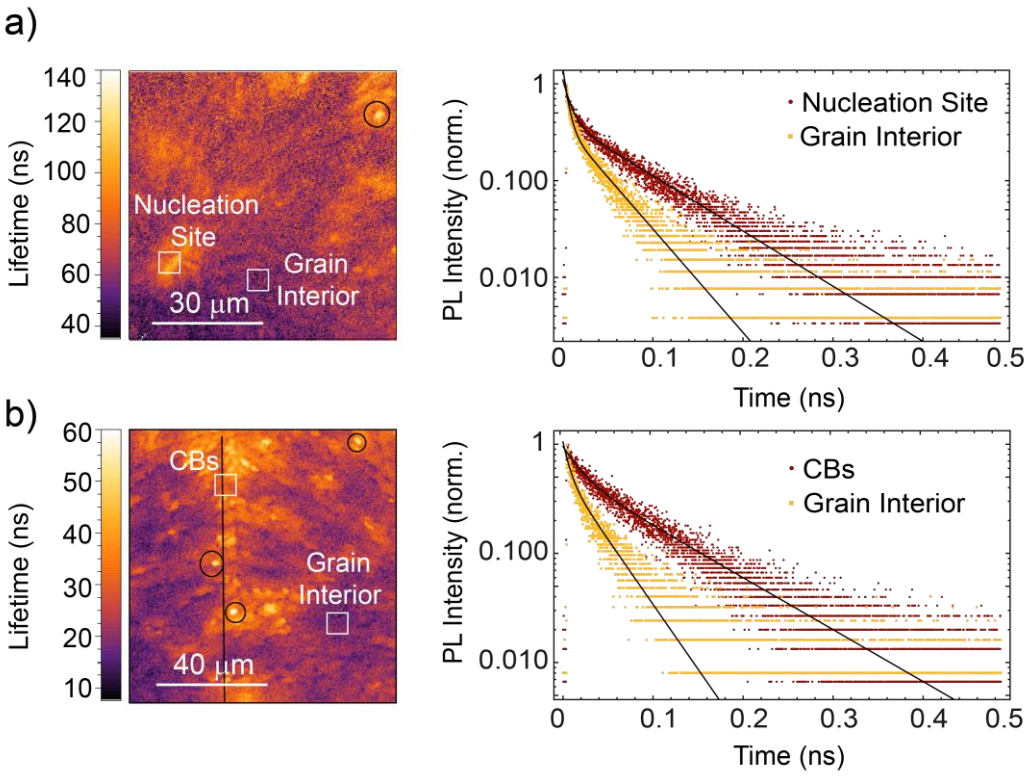

Figure S10. Lifetime maps of FIRA sample of the **a)** nucleation site and the **b)** CBs and corresponding decay curves of grain interior (darker) and CBs/nucleation site regions (brighter). For a) $\tau_{1,grain} = 5 \pm 0.2, \tau_{2,grain} = 40 \pm 0.4$ and $\tau_{1,nucleation} = 8.2 \pm 0.2, \tau_{2,nucleation} = 76.1 \pm 0.6$, for b) $\tau_{1,grain} = 6.8 \pm 0.4, \tau_{2,grain} = 36.5 \pm 0.6$ and $\tau_{1CBs} = 8.6 \pm 0.8, \tau_{2,nucleation} = 91.2 \pm 1.1$. Throughout the cluster the lifetime is comparable and neither shortening nor lengthening of lifetime is observed at the GBs within the FIRA cluster, while we observe longer slow component at the CBs and some long-lived hotspots. Lines represent the cluster boundaries and the long-lived hotspots are circled in black.

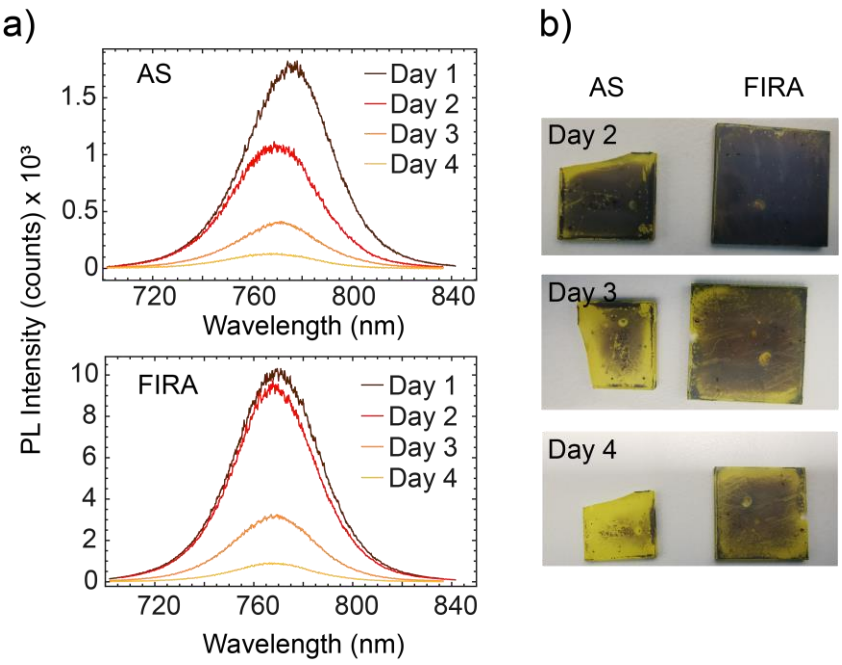

Figure S11. PL spectra of **a)** AS and FIRA measured after fabrication and up to 4 days of exposure to ambient conditions (with relative humidity of 22±4 RH% and temperature of 21±2 °C). **b)** Images of AS and FIRA films after 2, 3 and 4 days of air exposure.

Supplementary Information S1 – EBSD data acquisition and analysis

a. Sample preparation and geometry of the setup

The samples were prepared and kept in a nitrogen-filled glovebox to prevent degradation from moisture exposure before the measurement. Samples were deposited on ITO to avoid charging. Samples were glued on a metallic stub with silver paste and left degassing for at least 2 hours in a humidity-controlled environment (<5%). Since the perovskite is a soft material, no additional mechanical treatments (e.g. mechanical polishing, grinding, electropolishing, ion milling) were applied before the measurement.

The sample was mounted at 70° with respect to the horizontal to maximize the collection yield of the backscattered electrons, and the detector is placed horizontally on the side a few centimeters away from the specimen as shown **in Figure S12**.

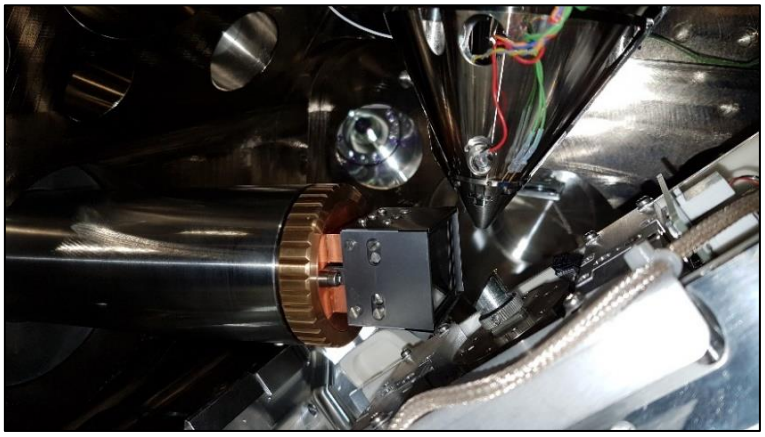

Figure S12. Geometry of the EBSD setup

b. Resolution of the system and depth probed

Our EBSD system has high angular resolution of about 0.5° and a direct detection system which allows for very low electron current, preventing sample damage. The system has been discussed extensively in a recent publication[1]. The angular resolution of EBSD is related to the quality and sharpness of the diffraction patterns and therefore how well a Kikuchi pattern can be indexed. The

spatial resolution of the EBSD is limited by the excitation volume which is the interaction volume of the primary electrons within the sample from which electrons are backscattered, forming the typical diffraction patterns. Using Monte Carlo-based simulation (CASINO[2]) and 15 keV as primary beam voltage, we estimate the 50% escape probability of electrons in the interaction volume to be from 35 nm below the surface for a 70° tilted sample. For a 0° tilted sample these electrons could escape from 260 nm below the surface (see **Figure S13**). Thus, tilting the sample makes EBSD a more surface sensitive technique.

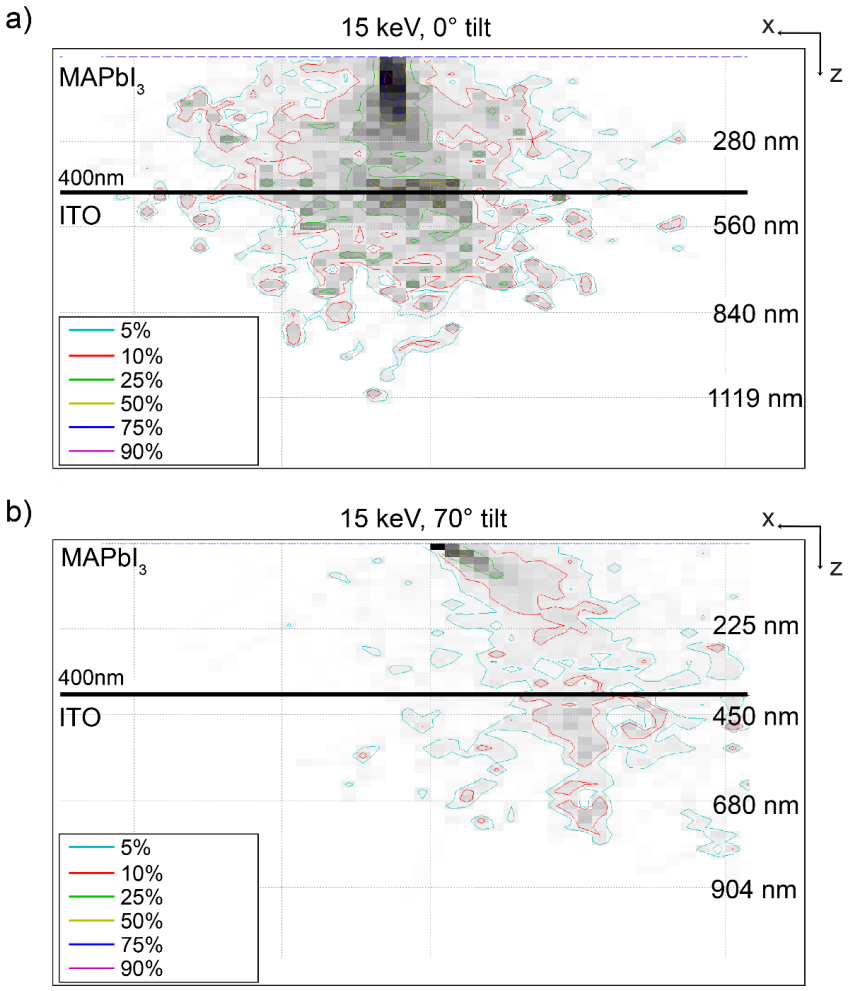

Figure S13. Simulated interaction volume between 15keV electron beam and 400nm $MAPbI_3$ perovskite on ITO obtained using a Monte Carlo simulator (CASINO). **a)** Interaction volume in the X-Z plane of back-scattered electron beam at 0° (no tilt applied) and **b)** 70° tilt (EBSD configuration).

The percentages shown represent the probability of back-scattering electrons from different positions in the sample (e.g. 50% of escape probability represented by the yellow line).

c. Image processing of Kikuchi patterns

To obtain Kikuchi lines, we use a Phyton script to average the background from at least 1000 Kikuchi patterns and divide the pattern from the measurement by this background to correct for spatial differences in collection efficiency. In addition, we apply brightness corrections to remove fluctuations of individual quadrant brightness from frame to frame (usually observed working at low beam current). The result of our image processing is shown in **Figure S14**.

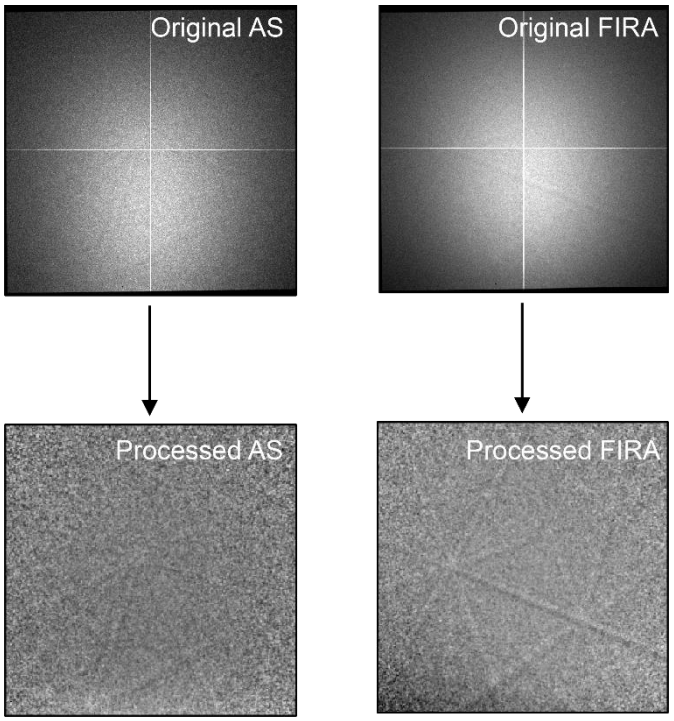

Figure S14. Original Kikuchi patterns for the AS and FIRA sample and the corresponding patterns after image processing.

d. Indexing of Kikuchi lines

Kikuchi patterns can be described as a gnomonic projection of the crystal lattice on the flat screen where the angles between the projected planes correspond to the interplanar angles, the band crossings to zone axes of the crystal lattice, and the width of the bands is related to the interplanar spacing, d_{hkl}, as follows from Bragg's law. Kikuchi bands are converted into points by the mathematical Hough's transformation as they are easier to locate and fit automatically. We index the Kikuchi patterns using OIM Analysis™ from EDAX. To index the Kikuchi patterns, it is necessary to input the correct crystal structure of the material (in our case tetragonal) and an accurate calibration. The latter is fundamental to obtain reliable data. The goal of the calibration is to establish the geometry of the projection of the EBSD pattern onto the detector and therefore determine the geometrical relationship between the sample coordinates in the SEM chamber and the detector. To calibrate our system, we use a routine which define the calibration parameters using a high-quality pattern from a known material at a specific working distance. Specifically, we have measured and indexed for 10 to 13mm as working distance Kikuchi patterns of copper and silicon. Then this calibration has been applied to perovskite Kikuchi patterns. To define the grains of AS and FIRA samples the deviation of a maximum 3° in the line position was allowed to consider two adjacent pixels from the same grain.

Supplementary Information S2

We simulate the expected PL spectra as a function of the additional travelled thickness (ATT) by the light before being emitted using the model following[3]

$$I_{emission}(d;\lambda) = I_{emission}(d_0;\lambda)e^{-\alpha(\lambda)d} \quad (1)$$

where $I_{emission}(0;\lambda)$ is the PL spectrum of the interior region of the cluster used as reference, d is the thickness by which light is transmitted within the perovskite, $\alpha(\lambda)$ is the absorption coefficient obtained from absorption, A(λ), as follows

$$\alpha(\lambda) = \frac{\ln(10)\, A(\lambda)}{d_0}$$

The model takes in account only the attenuation of the emitted light due to self-absorption events. In **Figure S15a** we show the agreement of the simulated PL spectrum with the experimental measured spectrum when the ATT is 250 nm. We convert the additional thickness transmitted by the light through the perovskite into the expected PL peak position by calculating equation (1). Therefore, we fit a second order polynomial to find the relation between the PL peak position and the ATT (**Figure S15b)**. Thus, experimental emission wavelengths of the FIRA cluster shown in Figure 4c in the main text are converted using the relation obtained.

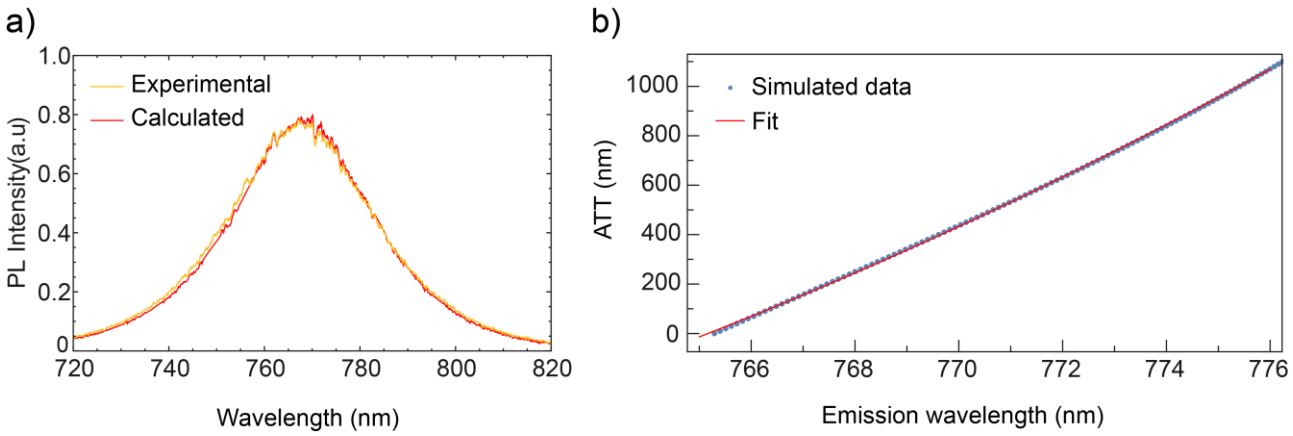

Figure S15. a) Experimental and simulated PL spectrum for additional transmitted thickness (ATT) of 250 nm. **b)** Relation between the PL peak position and the ATT before light being emitted.

Supplementary Information S3

The elongation of this radiative decay component due to photon recycling events has been observed in earlier works[1–3]. From Staub et al[1]., the externally observed bimolecular component ratio is given by

$$k_{ratio}^{ext} = \frac{1 - p_{r,0}k}{1 - p_{r,CB}k}$$

Where k is the radiative fraction, p_r is the probability for a photon to be reabsorbed in the layer before being emitted

$$p_r = 1 - p_e - p_p$$

and p_e is the probability for a photon to be emitted without reabsorption events which depends on the escape cone Ω, and p_p is parasitic absorption into the substrate.

Assuming the radiative fraction k and p_p are constant, the radiative lifetime ratio at the grain interior and at the grain boundaries would only depend on the sample thickness and the escape cone

$$\frac{\tau_0}{\tau_{CB}} \approx \frac{1 - \left(\frac{p_{e,0}}{d_0} d\Omega_0 + \frac{p_{a,0}}{d_{CB}}\right) k}{1 - \left(\frac{p_{e,CB}}{d_{CB}} d\Omega_{CB} + \frac{p_{a,0}}{d_{CB}}\right) k}$$

where d_0 and d_{CB} are the thickness at the grain interior and at the cluster boundaries, respectively. $d\Omega_0$ and $d\Omega_{CB}$ are the escape cone at the grain and at the grain boundaries.

Experimentally we find the lifetime ratio to be 1.5.

Accounting only for differences in thickness, the value obtained is overestimated compared to the one observed experimentally. Light-outcoupling is favored by the difference in roughness surfaces. On average the grain interior and the cluster boundary regions show RMS roughness of 26.8±14.5 nm and 75.3±21 nm, respectively. Therefore, for the CBs, the $d\Omega_{CB}$ is increased and the lifetime ratio decreases in accordance with experimental observations.

Supplementary Information S4

The distance crossed by the charges is limited by the charge carrier diffusion coefficient and half the oscillation period ν (8.5 GHz), and the probing length *P* is given by:

$$P = \sqrt{\mu (k_B T/e) \frac{1}{2} \upsilon^{-1}}$$

Figure S16 shows the probing length at room temperature as function of mobility for different measurement frequencies.[4]

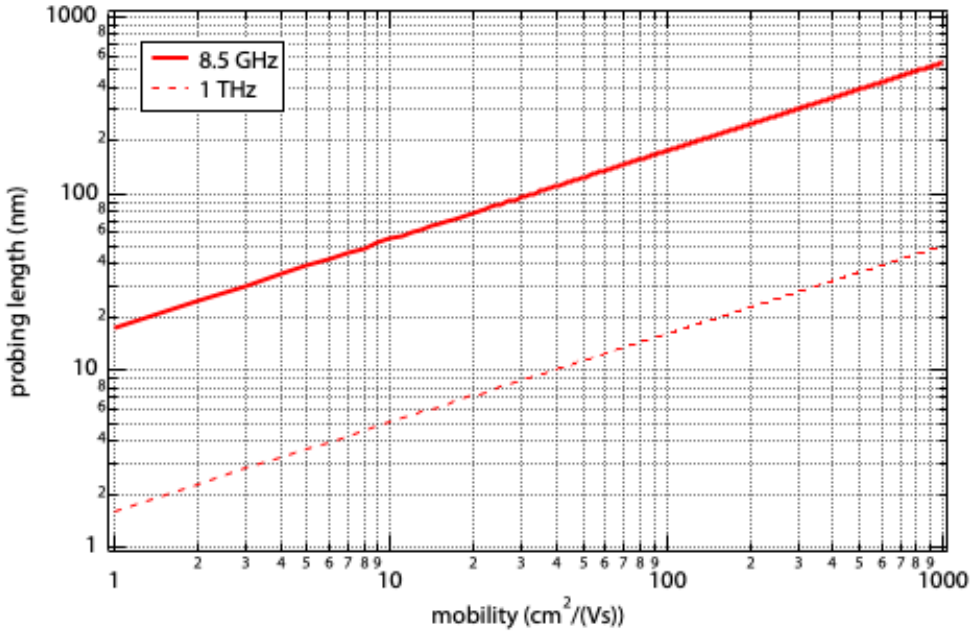

Figure S16. Probing length as function of mobility for photoconductivity measurements conducted at a frequency of 8.5 GHz (solid line, TRMC technique). This shows that the mobilities of 15 $cm^2/(Vs)$ and 19 $cm^2/(Vs)$ correspond to probing lengths of 68 nm and 76 nm, respectively. The probing length at 1 THz (dotted line, THz).

If we now assume a 300 nm-sized grain in which the charges are homogeneously distributed, then ~83% of the charges will be generated within the TRMC probing length of 68 nm of a grain boundary. For a grain size of 10 μm, this would be less than 5%. Hence, the extremely similar lifetimes of mobile charges for the different grain sizes means that the recombination is not significantly affected by the surface.

References

(1) Adhyaksa, G. W. P.; Brittman, S.; Āboliņš, H.; Lof, A.; Li, X.; Keelor, J. D.; Luo, Y.; Duevski, T.; Heeren, R. M. A.; Ellis, S. R.; et al. Understanding Detrimental and Beneficial Grain Boundary Effects in Halide Perovskites. *Adv. Mater.* **2018**, *30* (52), 1804792.

(2) Demers, H.; Poirier-Demers, N.; Couture, A. R.; Joly, D.; Guilmain, M.; de Jonge, N.; Drouin, D. Three-Dimensional Electron Microscopy Simulation with the CASINO Monte Carlo Software. *Scanning* **2011**, *33* (3), 135–146.

(3) Mohan, V.; Jain, P. K. Spectral Heterogeneity of Hybrid Lead Halide Perovskites Demystified by Spatially Resolved Emission. *J. Phys. Chem. C* **2017**, *121* (35), 19392–19400.

(4) W. Crothers, T.; L. Milot, R.; B. Patel, J.; S. Parrott, E.; Schlipf, J.; Müller-Buschbaum, P.; B. Johnston, M.; M. Herz, L. Photon Reabsorption Masks Intrinsic Bimolecular Charge-Carrier Recombination in CH3NH3PbI3 Perovskite. *Nano Lett.* **2017**, *17* (9), 5782–5789.

(5) Staub, F.; Kirchartz, T.; Bittkau, K.; Rau, U. Manipulating the Net Radiative Recombination Rate in Lead Halide Perovskite Films by Modification of Light Outcoupling. *J. Phys. Chem. Lett.* **2017**, *8* (20), 5084–5090.

(6) Diab, H.; Arnold, C.; Lédée, F.; Trippé-Allard, G.; Delport, G.; Vilar, C.; Bretenaker, F.; Barjon, J.; Lauret, J.-S.; Deleporte, E.; et al. Impact of Reabsorption on the Emission Spectra and Recombination Dynamics of Hybrid Perovskite Single Crystals. *J. Phys. Chem. Lett.* **2017**, *8* (13), 2977–2983.